



AIAA 2002-2745

Boundary Layer Transition Correlations
and Aeroheating Predictions for
Mars Smart Lander

Brian R. Hollis and Derek S. Liechty
NASA Langley Research Center
Hampton, VA

**32nd AIAA Fluid Dynamics
Conference and Exhibit**
24-26 June 2002
St. Louis, Missouri

For permission to copy or republish, contact the copyright owner named on the first page.
For AIAA-held copyright, write to AIAA Permissions Department,
1801 Alexander Bell Drive, Suite 500, Reston, VA, 2091-4344.

Boundary Layer Transition Correlations and Aeroheating Predictions for Mars Smart Lander

Brian R. Hollis* and Derek S. Liechty†
 NASA Langley Research Center, Hampton, VA 23681

Laminar and turbulent perfect-gas air, Navier-Stokes computations have been performed for a proposed Mars Smart Lander entry vehicle at Mach 6 over a free stream Reynolds number range of $6.9 \times 10^6/m$ to $2.4 \times 10^7/m$ ($2.1 \times 10^6/ft$ to $7.3 \times 10^6/ft$) for angles-of-attack of 0-deg, 11-deg, 16-deg, and 20-deg, and comparisons were made to wind tunnel heating data obtained at the same conditions. Boundary layer edge properties were extracted from the solutions and used to correlate experimental data on the effects of heat-shield penetrations (bolt-holes where the entry vehicle would be attached to the propulsion module during transit to Mars) on boundary-layer transition. A non-equilibrium Martian-atmosphere computation was performed for the peak heating point on the entry trajectory in order to determine if the penetrations would produce boundary-layer transition by using this correlation.

Nomenclature

a_w	speed of sound at wall (m/s)	T_∞	free stream temperature (K)
D	diameter (m)	U_∞	free stream velocity (m/sec)
H_{AW}	adiabatic enthalpy (J/kg)	w	penetration diameter (cm)
H_w	wall enthalpy (J/kg)	α	angle-of-attack (deg)
H_0	total enthalpy (J/kg)	δ	boundary layer thickness (m)
h	heat transfer coefficient (kg/m ² /sec), $h = q / (H_{AW} - H_w)$	ϕ	model rotation (deg)
h_{FR}	Fay-Riddell heat transfer coefficient (kg/m ² /sec)	Δs	wall cell height (m)
M_∞	free stream Mach number	μ_w	wall cell viscosity (kg/m/s)
M_e	boundary layer edge Mach number	ρ_∞	free stream density (kg/m ³)
p_∞	free stream pressure (N/m ²)	ρ_w	wall cell density (kg/m ³)
q	heat transfer rate (W/m ²)		
r	radial position (m)		
R	base (maximum) radius (m)		
R_n	nose radius (m)		
R_c	corner radius (m)		
Re_∞	free stream unit Reynolds number (1/m)		
$(Re_{w,e})_{turb}$	critical Reynolds number for turbulence, $(Re_{w,e})_{turb} = (\rho_e U_e w) / \mu_e$		
Re_{cell}	wall cell Reynolds number, $Re_{cell} = (\rho_w a_w \Delta s) / \mu_w$		
Re_θ	boundary layer momentum thickness Reynolds number, $Re_\theta = (\rho_e U_e \theta) / \mu_{we}$		

Introduction

The Mars Smart Lander (MSL) mission (Refs. 1 and 2) is intended to demonstrate an entry into the Martian atmosphere with an uncertainty in landing coordinates of less than 10 km. One of the important design issues for this vehicle is the determination of whether the boundary layer on the forebody of the entry vehicle will be laminar or turbulent. This determination is more complicated than has been the case for previous Mars missions because the MSL forebody will not have a smooth, unbroken surface; instead there will be six, circular penetrations in the forebody heat shield where bolts will be used to attach the vehicle to a cruise stage during transit from Earth.

The goal of the present study was to formulate transition criteria for the MSL which account for penetration diameter, penetration location, angle-of-attack, and Reynolds number. To accomplish this goal, wind tunnel testing was conducted in order to generate a transition database for these parametrics, and then Navier-Stokes computations were performed for the wind tunnel conditions in order to determine boundary-layer edge quantities which were used to correlate the transition data. The computations and correlations

* Aerospace Technologist, Senior Member AIAA

† Aerospace Technologist

Copyright © 2002 by the American Institute of Aeronautics and Astronautics, Inc. No copyright is asserted in the United States under Title 17, U.S. Code. The U.S. Government has a royalty-free license to exercise all rights under the copyright claimed herein for Governmental purposes. All other rights are reserved by the copyright owner.

are presented in this paper, while the wind tunnel data are presented in the companion paper by Liechty in Ref. 3. Comparisons of both laminar and turbulent aeroheating predictions with the experimental data are also presented, as are predictions for the peak heating condition during Mars entry.

A detailed investigation of the MSL aeroheating environment during Mars entry is presented by Edquist in Ref. 4. A similar study on penetration effects was performed for the Genesis mission, and is reported in Ref. 5.

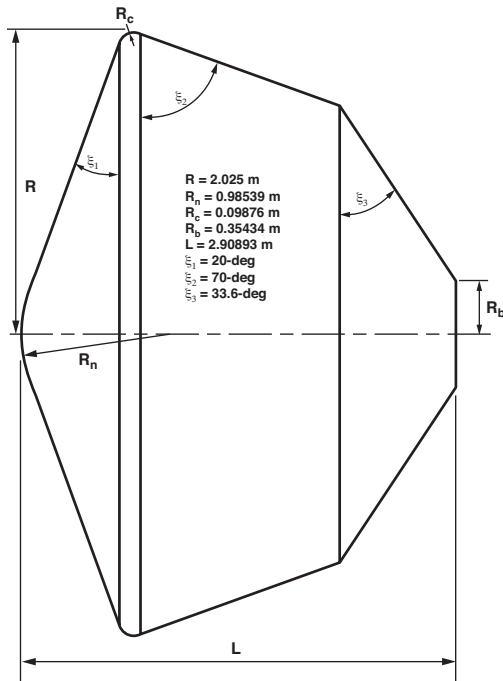


Figure 1: Dimensions of Full-Scale Mars Smart Lander Entry Vehicle

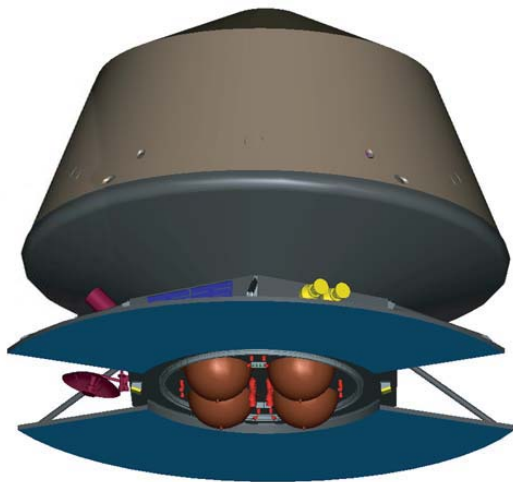


Figure 2: Mars Smart Lander and Cruise Stage

Mars Smart Lander Geometry

The proposed Mars Smart Lander entry vehicle is a 70-deg half-angle sphere-cone with a biconic afterbody (Fig. 1). The forebody will have six penetrations spaced at 60-deg increments where it will be bolted to the carrier vehicle in transit to Mars (Fig. 2). In this study, various penetration diameters and radial and angular positions were investigated in order to determine their effects on boundary layer transition and surface aeroheating levels.

Computational Method

Computations were performed using the LAURA (Refs. 6 and 7) code (version 4.9.2). The LAURA (Langley Aerothermodynamic Upwind Relaxation Algorithm) code is a three-dimensional, finite-volume solver which includes perfect-gas, equilibrium and non-equilibrium chemistry models. The code can be used to solve the inviscid, thin-layer Navier-Stokes, or full Navier-Stokes equations. For the current study the thin-layer mode was employed; it was concluded in Ref. 5 from computations on a similar blunt body that this mode provided accurate results for attached forebody flows. Time integration to steady-state in LAURA is accomplished through a point-relaxation scheme. Roe-averaging (Ref. 8) with Harten's entropy fix (Ref. 9) and Yee's Symmetric Total Variation Diminishing limiter (Ref. 10) is used for inviscid fluxes, and a second-order scheme is employed for viscous fluxes. For turbulent computations, the algebraic Baldwin-Lomax (Ref. 11) model with modifications (Ref. 12) for compressible flow and the Dhawan-Narashima (Ref. 13) transition model were employed. In this study, the perfect-gas air model was used for the wind tunnel computations, and an 8-species non-equilibrium, non-ionizing Martian atmosphere model (CO_2 , CO , N_2 , O_2 , NO , C , N , O) was used for the flight case.

Free stream conditions for the LAURA wind tunnel computations were set to the nominal free stream operating conditions of the NASA Langley Research Center (LaRC) 20-Inch Mach Air Tunnel, which are listed in Table 1. For the wind tunnel computations, a uniform, ambient 300 K wall temperature boundary condition was imposed. The use of a constant wall temperature is valid because the experimental data are reported in terms of the non-dimensional ratio, h/h_{FR} , which is assumed to remain constant with wall temperature. The quantity h_{FR} is the heat-transfer coefficient computed using the Fay-Riddell (Ref. 14) method with the same nose radius as the MSL model at a wall temperature of 300 K (540 °R).

For the flight case, free stream conditions were taken from the peak heating point on the nominal trajectory and are listed in Table 2. The wall boundary condition was set to “super-catalytic” (full recombination to free stream concentrations) with a radiative equilibrium wall temperature and a wall emissivity of 0.90.

A structured, finite-volume, multiple-block grid with a singularity-free nose was employed for the computations. Although the grid completely encompassed the afterbody and wake, computations were limited to the forebody blocks as this was the region of interest in the present study. The forebody grid blocks contained approximately 230,000 points with a body-normal (k -index) resolution of 65 points. Grid adaptation was performed (as per the method detailed in Ref. 7) to align the grid with the bow shock and to produce nominal wall cell Reynolds numbers on the order of $Re_{cell} = 10$.

The effects of normal grid-point resolution on the computed heating distributions was examined by repeating the computations for the $\alpha = 16$ -deg, $Re_\infty = 1.9 \times 10^7/m$ case with grids containing half (32) and twice (128) as many cells in the normal direction as the nominal grid (64). The heating distributions from these computations are shown in Fig. 3. Heating levels dropped nearly uniformly over the entire surface by about 5% from the 32-cell grid to the 64-cell grid, but from the 64-cell grid to the 128-cell grid, heating levels dropped by about 1% except around the stagnation region, where the decrease was approximately 2%. Therefore, it was concluded that the original 64 normal cell grid provided acceptable accuracy for this study.

Although the wind tunnel test models were fabricated with actual penetrations to replicate those in the

flight vehicle heat shield, the MSL computational grid did not include these penetrations. Thus, the effects of the penetrations on the flow field were not modeled in the computations. The effects of the penetrations on the state of the boundary layer were simulated by specifying that transition began at the penetration location. In order to attempt to bound the effects of the penetrations on boundary layer transition, the transition length in the Dhawan-Narashima transition model was specified as either zero, to simulate an immediate jump to fully-developed turbulent flow, or as equal to the running length of the boundary layer from the nose of the vehicle to the penetration location to simulate natural transition.

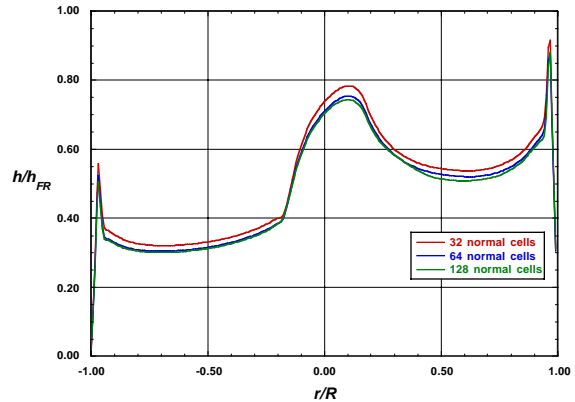


Figure 3: Effects of Normal Grid Resolution on Computed Heating Levels, $\alpha = 16$, $Re_\infty = 2.4 \times 10^7/m$

Table 1: Free Stream Conditions for Wind Tunnel Cases

Re_∞ (1/m)	M_∞	T_∞ (K)	ρ_∞ (kg/m ³)	U_∞ (m/s)	h_{FR} (kg/m ² -s)	q_{FR} (W/cm ²)
6.7×10^6	5.95	62.0	3.35×10^{-2}	938.6	0.283	5.70
8.5×10^6	5.97	62.2	4.05×10^{-2}	943.0	0.313	6.45
9.8×10^6	5.98	62.2	4.62×10^{-2}	944.4	0.335	6.95
1.1×10^7	5.99	61.6	5.29×10^{-2}	940.1	0.356	7.25
1.4×10^7	6.00	61.3	6.41×10^{-2}	940.4	0.392	7.95
1.7×10^7	6.02	63.4	7.92×10^{-2}	958.7	0.446	9.92
1.9×10^7	6.03	62.8	8.99×10^{-2}	955.6	0.474	10.4
2.4×10^7	6.06	62.3	1.13×10^{-1}	954.6	0.529	11.5

Table 2: Free Stream Conditions at Peak Heating

Time (sec)	163
Alt. (km)	37.1
U_∞ (m/s)	4919
ρ_∞ (kg/m ³)	4.15×10^{-4}
T_∞ (K)	159.3
M_∞	24.7
Re_∞ (1/m)	2.57×10^5

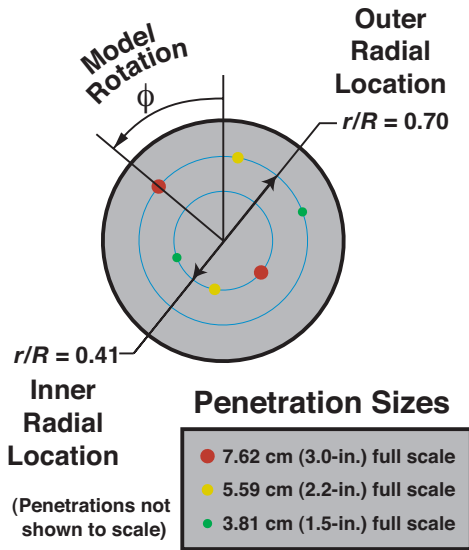


Figure 4: Layout of Penetrations on MSL Model

Experimental Method

The wind tunnel test which complements this computational study is presented in detail in Ref. 3, and a brief discussion is included herein for completeness.

Aeroheating tests were conducted in the NASA LaRC 20-Inch Mach 6 Air Tunnel. This facility is a blow-down tunnel in which heated, dried, and filtered air is used as the test gas. The tunnel has a two dimensional, contoured nozzle which opens into a 0.521 m x 0.508 m (20.5-in. x 20.0-in.) test section. The tunnel is equipped with a bottom-mounted injection system which can transfer a model from the sheltered model box to the tunnel centerline in less than 0.5 sec. Run times of up to 15 minutes are possible in this facility, although for the current aeroheating study, run times of only a few seconds were required. The nominal reservoir conditions of this facility are stagnation pressures of 206.8 to 3447.4 kPa (30 to 500 psia) with stagnation temperatures of 422.2 to 555.5 K (760 °R to 1000 °R),

which produce perfect-gas free stream flows with Mach numbers between 5.8 and 6.1 and Reynolds numbers of $1.64 \times 10^6 \text{ m}^{-1}$ to $23.3 \times 10^6 \text{ m}^{-1}$ ($0.5 \times 10^6 \text{ ft}^{-1}$ to $7.3 \times 10^6 \text{ ft}^{-1}$). A more detailed description of this facility is presented in Refs. 15 and 16. Representative flow conditions for each of the standard 20-Inch Mach 6 Air Tunnel operating points have been computed using the GASPROPS (Ref. 17) code and are listed in Table 1.

Global surface heating distributions were obtained using the digital optical measurement method of two color, relative-intensity, phosphor thermography (Refs. 18-21). In this method, ceramic wind tunnel models are coated with a phosphor compound which fluoresces in two separate regions (green and red) of the visible light spectrum. Before and during a wind tunnel run, the phosphor-coated model is illuminated by ultraviolet (UV) light sources, and the resulting fluorescent intensity of the model is recorded and digitized through a three-color CCD (charge coupled device) camera. Intensity data are converted to surface temperature values using system calibrations. Global heat-transfer distributions are then computed from these temperature data using one-dimensional, constant heat-transfer coefficient, conduction theory. As discussed in Ref. 3, the estimated experimental uncertainty of the heating data is approximately $\pm 13\%$.

The heating data are presented in the non-dimensional form, h/h_{FR} , where h_{FR} is the reference heat-transfer coefficient from Fay-Riddell theory for a 300 K (540 °R) surface temperature and the nose radius of the model. In the definitions of both h and h_{FR} , the adiabatic wall enthalpy, H_{aw} , is assumed to be equal to the total enthalpy, H_0 .

Heating distributions were measured on 0.0314-scale ceramic models of the MSL entry vehicle. Model parametrics were: penetration diameter ($w = 7.62 \text{ cm} / 3.0\text{-in.}, 5.59 \text{ cm} / 2.2\text{-in.},$ or $3.81 \text{ cm} / 1.5\text{-in.}$ full scale); angular location of the penetration (with respect to the leeside centerline); and radial location of the penetration ($r/R = 0.41$ or 0.70). These parametrics are shown in Fig. 4. Note that the actual flight vehicle would have six penetrations of uniform diameter at a constant radial location separated by 60-deg rotational increments.

Aeroheating Predictions and Comparisons with Experimental Data

Laminar Comparisons

Laminar computations were performed at the conditions listed in Table 1 for angles-of-attack of 0-deg, 11-deg, 16-deg, and 20-deg. Symmetry plane

comparisons of these computed heating distributions with the wind tunnel data for each angle-of-attack are presented in Figs. 5-8. In these figures, the experimental data shown were measured on models without penetrations on the symmetry line. The computed laminar heating distributions were found to agree with the experimental data to within the estimated uncertainty for all cases except at the forebody corners.

Turbulent Comparisons

Turbulent computations were performed for wind tunnel conditions of $Re_\infty = 1.4 \times 10^7/m$ to $2.4 \times 10^7/m$ at $\alpha = 16$ -deg, which is the nominal angle-of-attack at peak heating on the flight trajectory. Because boundary layer transition in the experiment was produced by penetrations in the test models (as it would also occur in flight) as opposed to naturally, transition in the computations was modeled in several different ways in order to attempt to model the data. Computations were performed with: the boundary layer fully turbulent over the length of the vehicle; natural transition beginning at the location of the penetration; and zero-length transition to fully-turbulent flow at the penetration location. For the natural transition computations, the transition length was set equal to the running length of the flow from the nose to the penetration.

Symmetry-plane comparisons of these computations with the experimental data for both radial penetration locations are shown for $r/R = 0.41$, $Re_\infty = 1.4 \times 10^7/m$, $1.9 \times 10^7/m$, and $2.4 \times 10^7/m$ in Figs. 9-11 and for the same Reynolds numbers with $r/R = 0.70$ in Figs. 12-14. In both sets of figures, comparisons are shown only for the lee-side of the vehicle because the wind-side penetration was observed to have little or no effect on the heating except at the penetration itself.

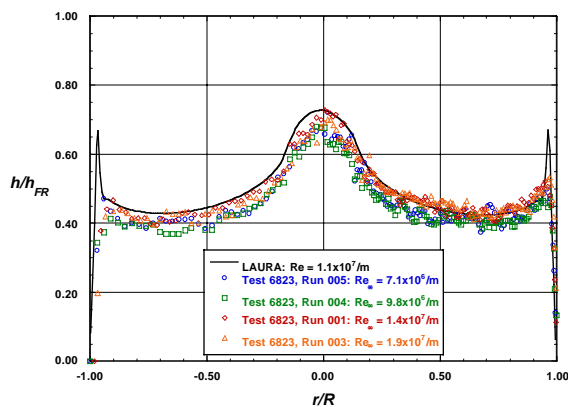


Figure 5: Laminar Centerline Heating Comparison for $\alpha = 0$ -deg

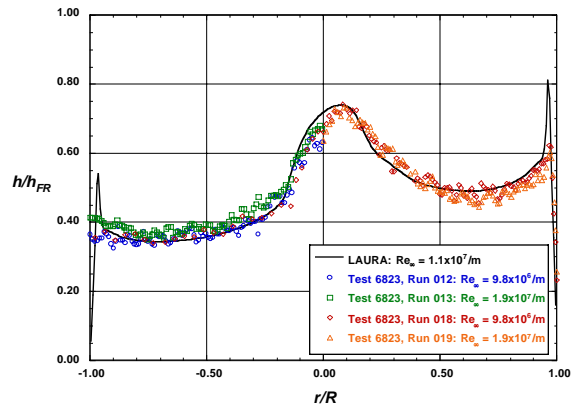


Figure 6: Laminar Centerline Heating Comparison for $\alpha = 11$ -deg

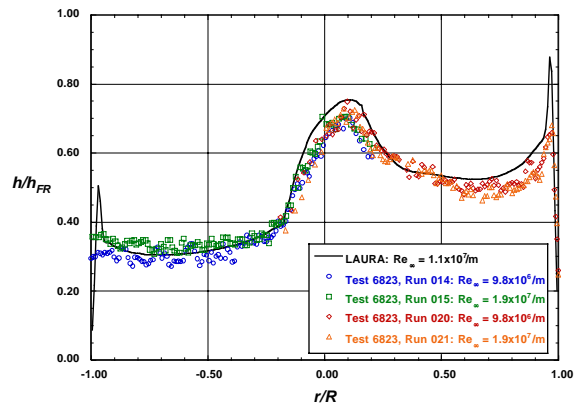


Figure 7: Laminar Centerline Heating Comparison for $\alpha = 16$ -deg

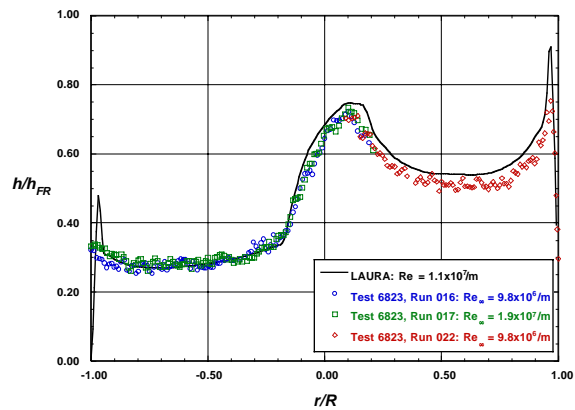


Figure 8: Laminar Centerline Heating Comparison for $\alpha = 20$ -deg

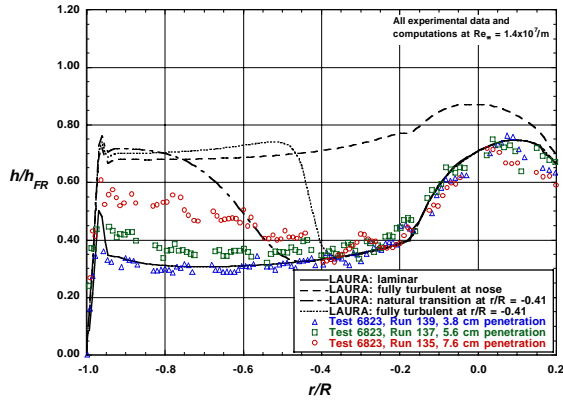


Figure 9: Turbulent Leeside Centerline Comparison for $\alpha = 16, Re_\infty = 1.4 \times 10^7/m, r/R = 0.41$

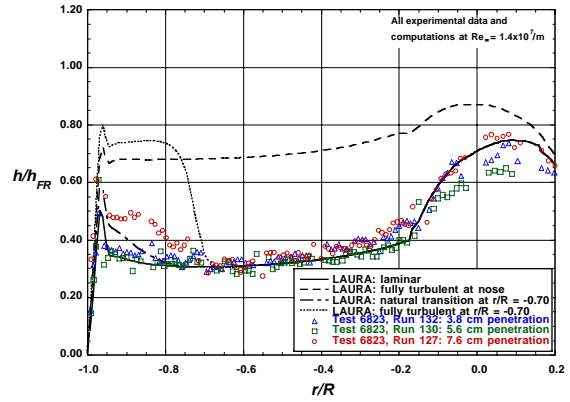


Figure 12: Turbulent Leeside Centerline Comparison for $\alpha = 16, Re_\infty = 1.4 \times 10^7/m, r/R = 0.70$

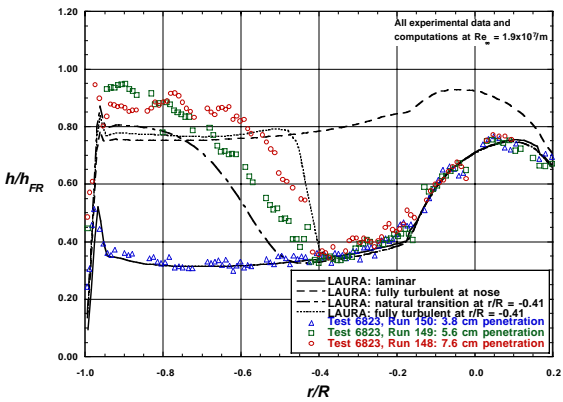


Figure 10: Turbulent Leeside Centerline Comparison for $\alpha = 16, Re_\infty = 1.9 \times 10^7/m, r/R = 0.41$

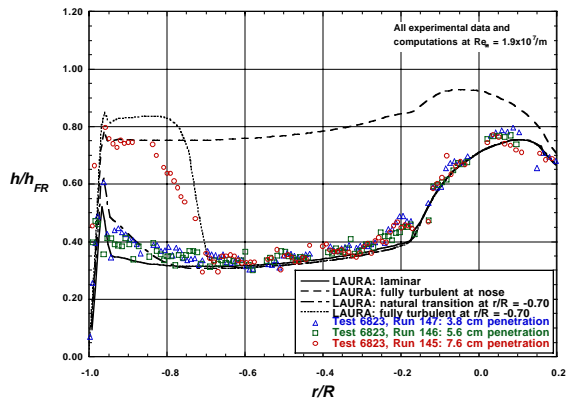


Figure 13: Turbulent Leeside Centerline Comparison for $\alpha = 16, Re_\infty = 1.9 \times 10^7/m, r/R = 0.70$

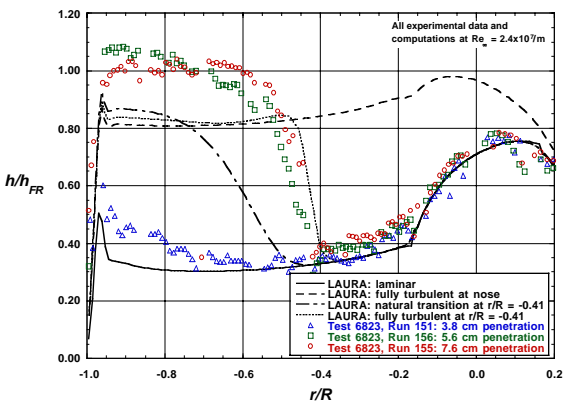


Figure 11: Turbulent Leeside Centerline Comparison for $\alpha = 16, Re_\infty = 2.4 \times 10^7/m, r/R = 0.41$

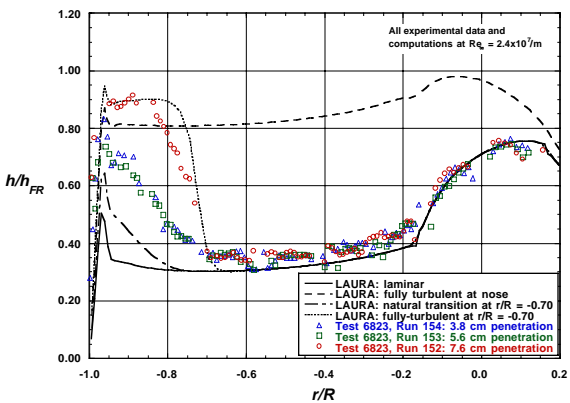


Figure 14: Turbulent Leeside Centerline Comparison for $\alpha = 16, Re_\infty = 2.4 \times 10^7/m, r/R = 0.70$

As shown in Figs. 9-14, the location at which transition was specified to begin, and the length of transition which was specified had significant effects on the computed heating levels. For both radial locations of transition onset, the heating levels computed by assuming fully-turbulent flow beginning at the specified radial position (i.e. zero-length transition) were higher than those computed when the flow was treated as fully turbulent from the nose of the vehicle. This difference was due to the fact the boundary layer thickness at a given location was greater for the fully turbulent flow from the nose because of the longer running length over which the turbulent boundary layer had to grow. Similarly, the boundary layer growth was greater when zero-length transition was specified at the penetration location than when natural transition was specified. Hence, for the penetration location of $r/R = 0.40$, the heating levels at the end of natural transition were higher than those for zero-length transition at the same location because of the thinner boundary layer. However, for the $r/R = 0.70$ penetration case, the boundary layer was still transitional at the shoulder of the vehicle when natural transition was specified, so comparison with the zero-transition length computation was not possible.

The comparisons between experimental and computations results were also very dependent on transition location and transition length, as well as on Reynolds number and penetration size.

Consider first the comparisons for the inner penetration location of $r/R = 0.41$ (Figs. 9-11). At the lowest Reynolds number of $Re_\infty = 1.4 \times 10^7/m$ (Fig. 9), the smallest penetration had no effect on the heating and the intermediate penetration had only a slight effect, and these two data sets compared well with the laminar computation. Although a more significant heating increase was produced by the largest penetration, the heating levels only rose gradually over the length of the vehicle and never reached a "plateau" typical of fully developed turbulent flow. For this case, the measured heating levels fell between the laminar and natural transition computations.

For $r/R = 0.41$ at the intermediate Reynolds number of $Re_\infty = 1.9 \times 10^7/m$ (Fig. 10), the data for the smallest penetration appeared to remain laminar and matched the laminar computation. The heating distributions for the two larger penetrations had shapes similar to the natural transition computation, but the peak values were higher than either the natural or zero-length transition computations by more than 15% to 20%, which was outside the range of experimental uncertainty.

For $r/R = 0.41$ at the highest Reynolds number, of $Re_\infty = 2.4 \times 10^7/m$ (Fig. 10), the beginning of transi-

tion was noted downstream of the smallest penetration, but the boundary layer did not appear to develop into fully-turbulent flow. The shapes of the heating distributions for the two larger penetrations were similar to the zero-length transition predictions, but the peak heating levels were again 15% to 20% higher than the computed values.

Consider next the comparisons for the outer penetration location of $r/R = 0.70$ (Figs. 12-14). These cases are not as well suited for comparison as the $r/R = 0.41$ cases, because the boundary layer did not have sufficient running length from the outer penetration for fully-turbulent flow to develop. Significant heating augmentation was observed in the experimental data for the largest hole size at all Reynolds numbers and for the two smaller holes at the highest Reynolds number. At $Re_\infty = 1.4 \times 10^7/m$, the heating data for the largest penetration fell between the natural and zero-length transition predictions. For the two higher Reynolds numbers, the large penetration heating distributions appeared to match the shape of the zero-length transition predictions. In terms of the heating levels, the $Re_\infty = 1.9 \times 10^7/m$ data were approximately 10% to 15% lower than the zero-length transition prediction, while the $Re_\infty = 2.4 \times 10^7/m$ data closely matched the prediction.

The present method for predicting turbulent heating levels, i.e. an algebraic turbulence model with a specified transition location and a transition length bounded between zero and the running length ahead of the transition location, appeared to bound the experimental heating data for the range of Reynolds numbers and penetration sizes for the $r/R = 0.70$ penetration location. However, for the $r/R = 0.41$ penetration location, the present method under-predicted the measured peak heating levels by up to 20%, although the shape of the heating distributions was approximately reproduced. It should be noted that the actual heat-shield penetrations were not included in the computational geometry, and their possible effects on the flow field (i.e. circulation within the penetrations, shocks at the lip of the penetrations, boundary layer separation and vortex formation downstream of the penetrations) may be the cause for these differences.

In a similar study (Ref. 5) for the Genesis mission, the cavity was modeled in the computations. It was found in that study that the presence of the cavity had significant effects both on heating around the cavity itself, where a localized spike in the heating levels was predicted, and downstream of the cavity, where heating levels lower than without the cavity were predicted. However, it was also concluded in that study that the simple algebraic transition/turbulence models used (the same as in this study) were not sufficient to resolve the

effects of the cavity even with the cavity included in the computational geometry.

In terms of design criteria, the worst-case for heating, based on the experimental data, would be a penetration at $r/R = 0.41$ of sufficient diameter to cause transition, because the boundary layer has greater running length downstream of the penetration for turbulent flow to develop than it would have for a penetration at $r/R = 0.70$. This case with an $r/R = 0.41$ penetration which produced transitional/turbulent flow is represented by the data for the two larger penetrations at $Re_\infty = 2.4 \times 10^7/m$ (Fig. 11). For this case, the turbulent experimental heating levels downstream of the penetration were approximately 25% higher than at the nose. These experimental heating levels were approximately 10% higher than the predicted fully-turbulent levels at the nose, and were approximately 20% higher than those predicted downstream of the penetration using the zero-length transition model.

Boundary Layer Transition Correlations

Laminar computations were performed with LAURA for the complete wind tunnel test range of angle-of-attack ($\alpha = 0$ -deg, 11-deg, 16-deg, and 20-deg) and Reynolds numbers ($Re_\infty = 6.7 \times 10^6/m$ to $2.4 \times 10^7/m$) in order to determine boundary layer edge properties (Re_θ and δ), which could be used to formulate a transition correlation from the experimental data. Sample values of Re_θ and δ are shown in Figs. 15-17 for the $Re_\infty = 2.4 \times 10^7/m$, $\alpha = 11$ -deg, 16-deg and 20-deg cases.

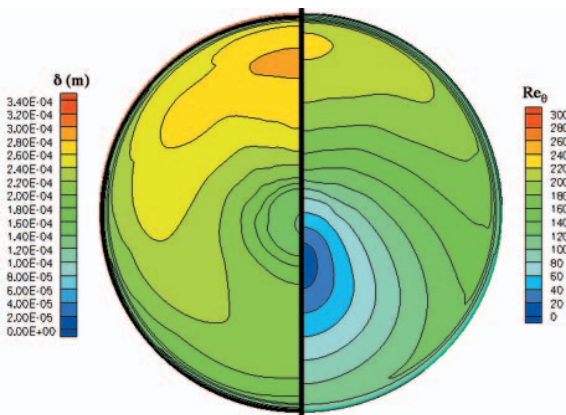


Figure 15: Re_θ and δ Distributions for $Re_\infty = 2.4 \times 10^7/m$, $\alpha = 11$ -deg

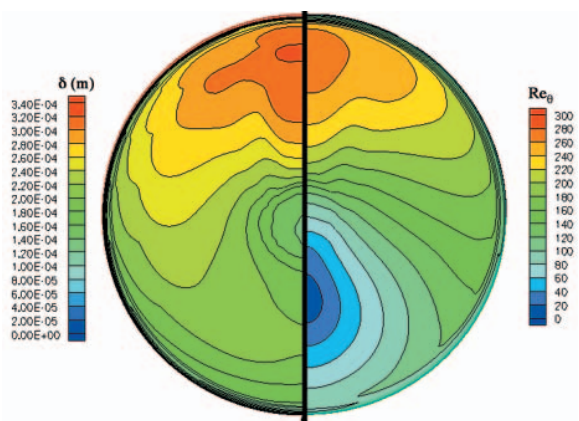


Figure 16: Re_θ and δ Distributions for $Re_\infty = 2.4 \times 10^7/m$, $\alpha = 16$ -deg

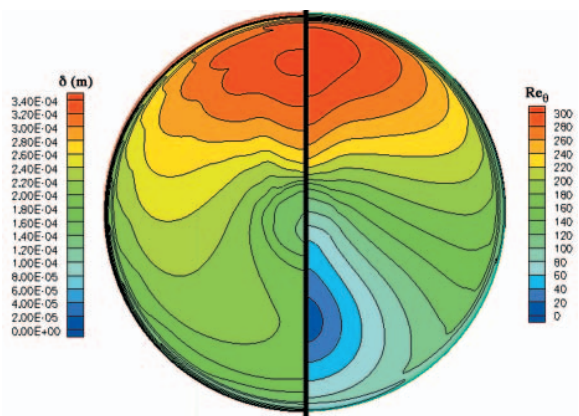


Figure 17: Re_θ and δ Distributions for $Re_\infty = 2.4 \times 10^7/m$, $\alpha = 20$ -deg

Approximately 800 data points on the state of the boundary layer which covered the range of angles-of-attack, free stream Reynolds numbers, penetration diameters, and penetration radial locations were obtained during the wind tunnel test. For each data point, the state of the boundary layer downstream of the penetration was determined through visual inspection of the surface heating images and classified as either: laminar; localized disturbance at penetration; transition downstream of penetration; or fully turbulent at penetration. Examples of experimental data which fit each of these classifications are shown in Fig. 18. These classifications are somewhat simplified descriptions of a complex flow field and should be used with care. For example, for a data point classified as “local disturbance”, the heating levels measured near the penetration may be higher than heating levels downstream of a penetration for a data point classified as “transition downstream”. Additionally, because of the three-dimensional nature of the flow over this geometry at angle-of-attack, transitional/turbulent heating levels downstream of a

penetration are highly dependent on the location of that penetration.

In order to determine which points would be used to generate correlations, the data were examined to determine at which value of Re_∞ fully turbulent flow at the penetration was first noted for fixed values of w , r/R and α . To define the turbulent boundary, these points were fitted to an equation of the form:

$$(Re_\theta)_{turb} = C(w/\delta)^{-1} \quad (1)$$

where the constant was found to be $C = 725$. Similarly, the values of Re_∞ at which laminar flow were last noted (for fixed values w , r/R and α) were fitted to an equation of the form:

$$(Re_\theta)_{lam} = C(w/\delta)^a \quad (2)$$

where $C = 3504$ and $a = -2.61$. The equations and the data to which they were fitted are shown in Fig. 19. Almost all of the turbulent data fell within the $\pm 20\%$ bands, but the laminar data showed more scatter.

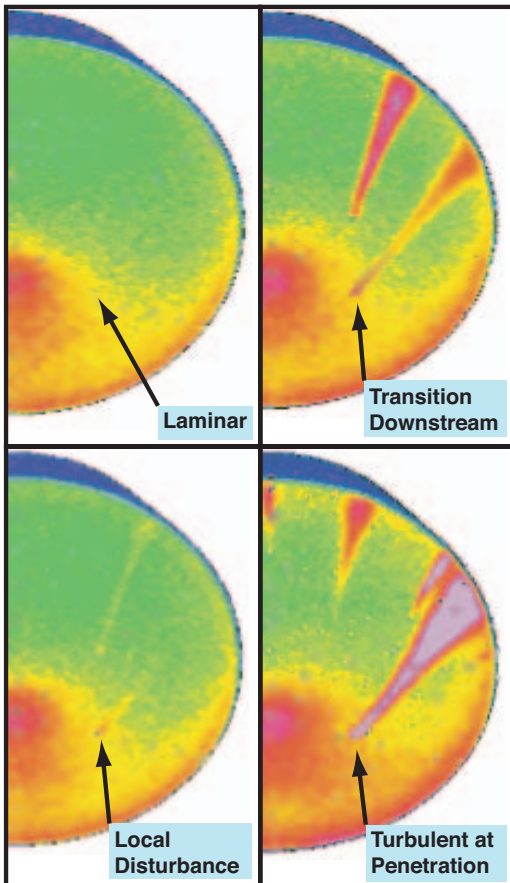


Figure 18: Classification of Penetration Effect on Boundary Layer

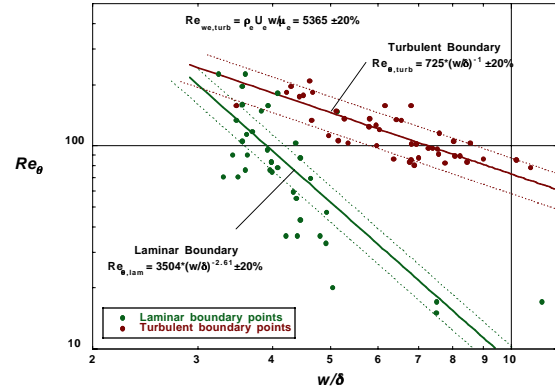


Figure 19: Curve Fits to Wind Tunnel Data Points on the Boundaries of Laminar and Turbulent Flow

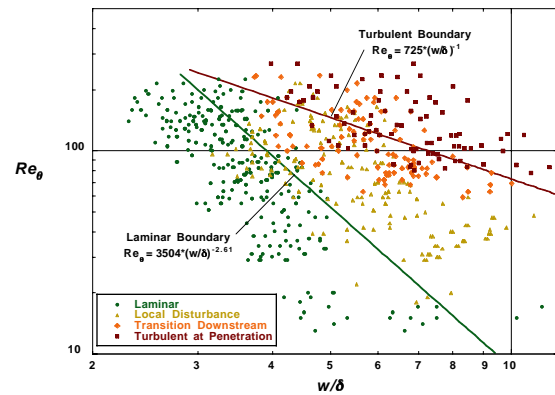


Figure 20: Entire Transition Data Set and Correlations for Laminar and Turbulent Boundaries

Having defined correlations for the end of laminar flow and the beginning of fully turbulent flow from the data points on the boundaries, these correlations are now shown with the entire data set in Fig. 20. Although there is some scatter, the majority of the “laminar” and “fully turbulent at penetration” data points fall below or above the respective curves, while the “local disturbance” and “transition downstream” data points fall between the two curves.

In Eq. 1, the exponent on the right-hand-side was fixed at -1 in order to determine a critical Reynolds number, as was first defined by Schiller (Ref. 22) and employed by many other authors (e.g. Refs. 23-26) to correlate transition data. Eq. 1 can be manipulated to yield:

$$(Re_{w,e})_{turb} = \frac{\rho_e U_e w}{\mu_e} = C \left(\frac{w}{\theta} \right) \left(\frac{\delta}{w} \right) = C \left(\frac{\delta}{\theta} \right) \quad (3)$$

For wind tunnel conditions, the ratio (δ/θ) is nearly constant (~ 7.4 for this geometry). With $C = 725$ and a $\pm 20\%$ error band, a critical Reynolds number,

based on boundary layer edge conditions and hole diameter, for immediate transition to fully turbulent flow at the penetration can then be given by:

$$(Re_{w,e})_{turb} \cong 5365 \pm 20\% \quad (4)$$

The boundary defined by this critical Reynolds number is shown for a sample case in Fig. 21.

It should also be noted that, based on past experience with blunt body transition (e.g. Ref. 27), a conservative limit for smooth-body transition in the absence of penetrations has been defined as $Re_\theta > 200$ for the MSL (Ref. 4). For design purposes, it is recommended that, in addition to the smooth-body transition criteria, the laminar boundary correlation (Eq. 2) be used to determine if heating effects due to a penetration need to be considered for a given flight condition because local heating effects at the penetration may still be significant even if transition does not occur.

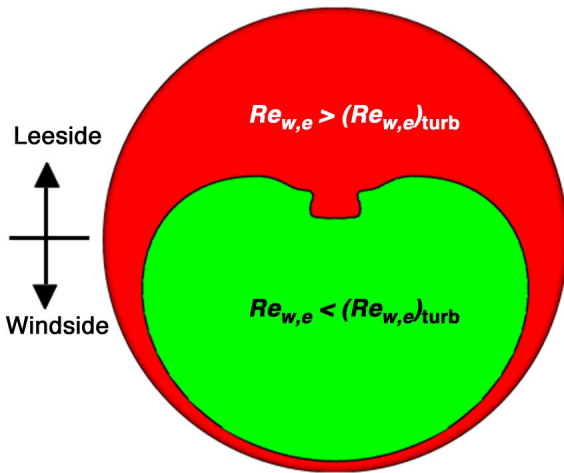


Figure 21: Critical Reynolds Number Boundary for $\alpha = 16$, $Re_\infty = 9.8 \times 10^6/m$, Largest Penetration Size

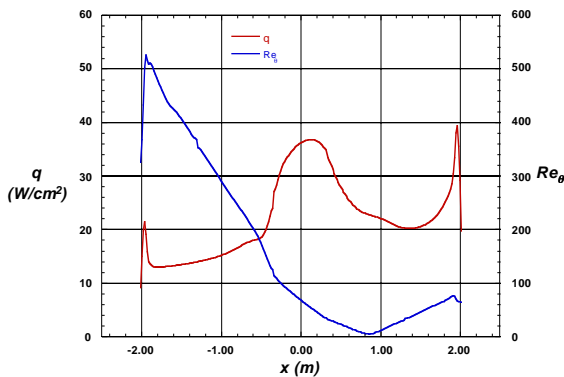


Figure 22: Centerline Heating and Re_θ Distributions for Peak Heating Point on Trajectory

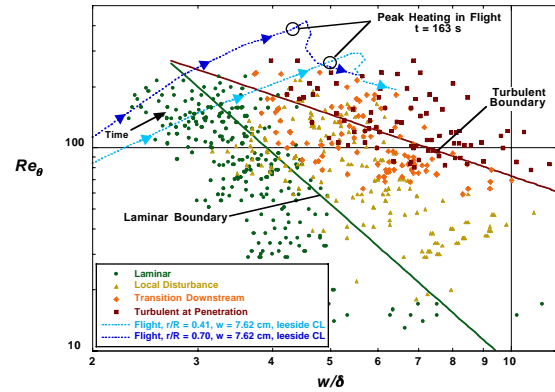


Figure 23: Trajectory Re_θ and δ Values Compared to Boundary-Layer Transition Data and Correlations

Flight Peak Heating Computation

A solution was computed for the peak heating point on the Mars entry trajectory (Table 2). The computed laminar heating and Re_θ centerline distributions are shown in Fig. 22. From the wind tunnel data, the worst-case parameters for heating were found to be the largest penetration diameter at the inner radial location ($r/R = 0.4$). For this case, the computed values of Re_θ and w/δ at peak heating were 263 and 5.0. For the outer radial location ($r/R = 0.70$), the values for Re_θ and w/δ were 382 and 4.3. In either case, the predicted values fell well above the fully-turbulent boundary from the correlation, and thus, turbulent heating at the penetration can be expected. Although not shown, the w/δ values for the two smaller penetrations also fell above the fully-turbulent boundary for both cases. Re_θ and w/δ values (and heating levels) were computed at several additional points along the trajectory in Ref. 4. These values are overlaid on the transition map in Fig. 23. Although this correlation was generated from data obtained in a perfect-gas air facility and may not be strictly applicable to non-equilibrium, Martian atmosphere conditions, the peak heating condition was found to be well above the turbulent border, and thus these results can be taken as a conservative estimate that accounting must be made for penetration-induced transition in the design of the MSL heat-shield

Summary

A computational and experimental study has been performed for the Mars Smart Lander in order to develop a correlation for the effects of heat shield penetrations on the state of the boundary layer and to compare predicted and measured wind tunnel heating levels.

Heating levels also were predicted for the peak heating point on the Mars entry trajectory.

Laminar Navier-Stokes predictions were found to agree with the laminar wind tunnel data to within the estimated experimental uncertainty of the data. The agreement in comparisons between turbulent Navier-Stokes predictions and experimental data was dependent on the location of transition in the experiment and the diameter of the penetration on the test model which produced the transition. In general, zero transition-length and natural transition-length turbulent predictions bounded the shape of the experimental heating distributions, but for the larger penetrations, the measured heating levels exceeded the predictions by more than 20%. These differences were attributed to the use of a simple algebraic turbulence model in the computations and the exclusion of the actual penetration (and hence its effects on the flow field) from the computational geometry.

Based on the turbulent experimental heating data, the worst-case heating levels were produced by the largest penetration size at the inner radial location: heating levels were 25% higher than the laminar heating level at the nose (from experiment or computation); 10% higher than the predicted fully-turbulent level at the nose; and 20% higher than the predicted zero-transition-length heating downstream of the penetration. In contrast, although transition at the outer radial location occurred at lower free stream Reynolds numbers than for the inner location, there was insufficient running length downstream of the penetration for fully turbulent flow to develop and so heating levels were lower. Thus, for aeroheating design considerations, an outer radial location for a penetration would be preferable.

Boundary layer edge quantities were extracted from the laminar Navier-Stokes solutions and were used to correlate the experimental data on the state of the boundary layer. The correlations were expressed in terms of Re_θ and w/δ , and can be used to determine if a heat-shield penetration will have no effect on the boundary layer, will have a local effect, will produce transition downstream of the penetration, or will cause immediate transition to turbulent flow. Computations for the peak heating case on the trajectory revealed that for all penetration diameters at both the inner and outer locations on the leeside, fully-turbulent flow would be produced downstream of the penetration.

Acknowledgements

The authors wish to thank the following persons at NASA LaRC for their contributions to this work: Karl Edquist and Peter Gnoffo for assistance with the

LAURA code; Steve Alter for generation of the computational grid; and Scott Berry for discussions on boundary-layer transition.

References

1. Lockwood, M. K., Powell, R. W., Graves, C. A., and Carman, G. L., "Entry System Design Considerations for Mars Landers," American Astronautical Society Paper AAS 01-023, 2001.
2. Lockwood, M. K., Sutton, K., Prabhu, R., Powell, R., Graves, C., and Epp, C., "Entry Configurations and Performance Comparisons for the Mars Smart Lander," AIAA 2002-4407, Aug. 2002.
3. Liechty, D. S. and Hollis, B. R., "Heat Shield Parametric Experimental Aeroheating for a Mars Smart Lander," AIAA Paper 2002-2746, 2002.
4. Edquist, K. and Loomis, M., "Aeroheating Environments for Mars Smart Lander Configurations," AIAA Paper 2002-4505, Aug. 2002.
5. Cheatwood, F. M., Merski, N. M., Riley, C. J., and Mitchletree, R. A., "Aerothermodynamic Environment Definition for the Genesis Sample Return Capsule," AIAA Paper 2001-2889, June 2001.
6. Gnoffo, P. A., "An Upwind-Biased, Point-Implicit Algorithm for Viscous, Compressible Perfect-Gas Flows," NASA TP-2953, Feb. 1990.
7. Cheatwood, F. M., and Gnoffo, P. A., "User's Manual for the Langley Aerothermodynamic Upwind Relaxation Algorithm (LAURA)," NASA TM 4674, April, 1996.
8. Roe, P. L., "Approximate Riemann Solvers, Parameter Vectors and Difference Schemes," *Journal of Computational Physics*, Vol. 43, No. 2, 1981, pp. 357-372.
9. Harten, A., "High Resolution Schemes for Hyperbolic Conservation Laws," *Journal of Computational Physics*, Vol. 49, No. 3, 1983, pp. 357-393.
10. Yee, H. C., "On Symmetric and Upwind TVD Schemes," NASA TM 88325, 1990.
11. Baldwin, B. S. and Lomax, H., "Thin Layer Approximation and Algebraic Model for Separated Turbulent Flow," AIAA Paper 78-257, Jan. 1978.

12. Cheatwood, F. M., and Thompson, R. A., "The Addition of Algebraic Turbulence Modeling to Program LAURA," NASA TM-107758, April 1993.
13. Dhawan, S., and Narashima, R., "Some Properties of Boundary Layer Flow from Laminar to Turbulent Motion," *Journal of Fluid Mechanics*, Vol. 1, Part 4, pp. 418-436, Jan. 1958.
14. Fay, J. A., and Riddell, F. R., "Theory of Stagnation Point Heat Transfer in Dissociated Air," *Journal of Aeronautical Sciences*, Vol. 25, No. 2., pp. 73-85, Feb. 1958.
15. Micol, J. R. "Hypersonic Aerodynamic/ Aerothermodynamic Testing Capabilities at Langley Research Center: Aerothermodynamic Facilities Complex," AIAA Paper 95-2107, June 1995.
16. Micol, J. R. "Langley Aerothermodynamic Facilities Complex: Enhancements and Testing Capabilities," AIAA Paper 98-0147, Jan. 1998.
17. Hollis, B. R., "Real-Gas Flow Properties for NASA Langley Research Center Aerothermodynamic Facilities Complex Wind Tunnels," NASA CR 4755, Sept. 1996.
18. Buck, G. M., "Automated Thermal Mapping Techniques Using Chromatic Image Analysis," NASA TM 101554, April 1989.
19. Buck, G. M., "Surface Temperature/Heat Transfer Measurement Using a Quantitative Phosphor Thermography System," AIAA Paper 91-0064, Jan. 1991.
20. Merski, N. R., "A Relative-Intensity, Two-Color Phosphor Thermography System," NASA TM 104123, Sept. 1991.
21. Merski, N. R., "Global Aeroheating Wind-Tunnel Measurements Using Improved Two-Color Phosphor Thermography Methods," *Journal of Spacecraft and Rockets*, Vol. 36, No. 2, pp. 160-170, March-April 1999.
22. Schiller, L., "Flow in Pipes", *Handbook of Experimental Physics*, Vol. 4, Pt. 4, Academic Press, Leipzig, Germany, 1932, pp. 189-192.
23. Reda, D. C., "Correlation of Nosetip Boundary-Layer Transition Data Measured in Ballistic Range Experiments," *AIAA Journal*, Vol 19, No. 3, 1981, pp. 329-339.
24. Poll, D. I. A., "The Effect of Isolated Roughness Elements on Transition in Attachment-Line Flows," *Laminar-Turbulent Transition*, edited by D. Arnal and R. Michel, Springer-Verlag, New York, 1990, pp. 657-667.
25. Bouslog, S. A., Bertin, J. J., Berry, S. A., and Caram, J. M., "Isolated Roughness Induced Boundary-Layer Transition: Shuttle Orbiter Ground Tests and Experience," AIAA Paper 97-0274, Jan. 1997.
26. Berry, S. A., Bouslog, S. A., Brauckmann, G. J., and Caram, J. M., "Shuttle Orbiter Experimental Boundary-Layer Transition Results with Isolated Roughness," *Journal of Spacecraft and Rockets*, Vol. 35, No. 3, 1998, pp. 241-248
27. Stetson, K. F., "Boundary-Layer Transition on Blunt Configurations," NASA-JSC-26528, Feb. 1994.